Atmos. Chem. Phys. Discuss., 14, 31627–31674, 2014
www.atmos-chem-phys-discuss.net/14/31627/2014/
doi:10.5194/acpd-14-31627-2014

Atmospheric Chemistry and Physics Discussions

Impact of planetary boundary layer turbulence on model climate and tracer transport

E. L. McGrath-Spangler[1,2], A. Molod[2,3], L. E. Ott[2], and S. Pawson[2]

[1]Universities Space Research Association, Columbia, MD, USA
[2]Global Modeling and Assimilation Office, NASA Goddard Space Flight Center, Greenbelt, MD, USA
[3]Earth System Sciences Interdisciplinary Center, University of Maryland, College Park, MD, USA

Received: 12 September 2014 – Accepted: 20 November 2014 – Published: 16 December 2014

Correspondence to: E. L. McGrath-Spangler (erica.l.mcgrath-spangler@nasa.gov)

Published by Copernicus Publications on behalf of the European Geosciences Union.

Abstract

Planetary boundary layer (PBL) processes are important for weather, climate, and tracer transport and concentration. One measure of the strength of these processes is the PBL depth. However, no single PBL depth definition exists and several studies have found that the estimated depth can vary substantially based on the definition used. In the Goddard Earth Observing System (GEOS-5) atmospheric general circulation model, the PBL depth is particularly important because it is used to calculate the turbulent length scale that is used in the estimation of turbulent mixing. This study analyzes the impact of using three different PBL depth definitions in this calculation. Two definitions are based on the scalar eddy diffusion coefficient and the third is based on the bulk Richardson number. Over land, the bulk Richardson number definition estimates shallower nocturnal PBLs than the other estimates while over water this definition generally produces deeper PBLs. The near surface wind velocity, temperature, and specific humidity responses to the change in turbulence are spatially and temporally heterogeneous, resulting in changes to tracer transport and concentrations. Near surface wind speed increases in the bulk Richardson number experiment cause Saharan dust increases on the order of 1×10^{-4} kg m^{-2} downwind over the Atlantic Ocean. Carbon monoxide (CO) surface concentrations are modified over Africa during boreal summer, producing differences on the order of 20 ppb, due to the model's treatment of emissions from biomass burning. While differences in carbon dioxide (CO_2) are small in the time mean, instantaneous differences are on the order of 10 ppm and these are especially prevalent at high latitude during boreal winter. Understanding the sensitivity of trace gas and aerosol concentration estimates to PBL depth is important for studies seeking to calculate surface fluxes based on near-surface concentrations and to studies projecting future concentrations.

ACPD
14, 31627–31674, 2014

1 Introduction

Aerosols exert control over the Earth's climate in several different ways. Directly, they affect the radiative budget through absorption and scattering of both shortwave and longwave radiation (Sokolik and Toon, 1996; Balkanski et al., 2007). Indirectly, they modify cloud reflectivity and lifetime through greater numbers of cloud condensation nuclei, smaller cloud droplets, and suppressed precipitation (Rosenfeld et al., 2001). Iron contained within aerosol dust enhances biological productivity when transported to the open ocean where it can change oceanic uptake of the greenhouse gas carbon dioxide (CO_2) through changes to marine photosynthesis (Fung et al., 2000; Jickells et al., 2005; Mahowald et al., 2009). Ventilation of tracers, such as dust, out of the planetary boundary layer (PBL) for transport downwind is dependent upon PBL turbulent mixing (Sinclair et al., 2008).

CO_2 has been increasing at a rate of 1–2 ppm year^{-1} (Conway et al., 1994) over the last half century. However, neither the processes controlling nor the locations of the sources and sinks of this greenhouse gas are understood (Davis et al., 2003). CO_2 inversion studies, which seek to estimate the magnitude and location of CO_2 fluxes, are negatively impacted by planetary boundary layer (PBL) depth uncertainty (Gurney et al., 2002; Gerbig et al., 2003; Baker et al., 2006) and this introduces uncertainty into estimates of global climate change.

Trace gases emitted at the surface are diluted through turbulent mixing in the PBL, and low PBL depths limit vertical mixing and favor higher accumulation of local pollutants near the surface (Pérez et al., 2010; McGrath-Spangler and Denning, 2010; Parrish et al., 2011). Vertical mixing within the PBL therefore affects the magnitude and temporal variability of surface concentrations and vertical mixing near the PBL top affects horizontal advection and downstream concentrations. These factors make accurate simulations of PBL mixing and depth critical for chemistry–transport models (Lin and McElroy, 2010).

ACPD
14, 31627–31674, 2014

Several studies have found that the estimated PBL depth varies with the definition used. Seidel et al. (2010) found that the PBL depth estimated using various definitions from a single atmospheric profile could differ by more than a kilometer and that the general differences among the definitions evaluated were on the order of hundreds of meters. Similarly, Vogelezang and Holtslag (1996) found that the formulation of the Richardson number, the inclusion of a surface friction velocity term, and the critical value of the Richardson number produced different estimates of PBL depth. Using the Goddard Earth Observing System (GEOS-5) model, McGrath-Spangler and Molod (2014) evaluated seven PBL depth definitions and found the largest variations in depth occur for the nocturnal boundary layer, and that the PBL depth estimated with Richardson number based methods are shallower than PBL depths estimated using methods based on the eddy diffusion coefficient. They also found that Richardson number based methods produce a shallower midday PBL under warm, moist conditions, such as in the tropical rainforest.

The GEOS-5 AGCM (atmospheric general circulation model) uses the PBL depth to inform the calculation of the turbulent length scale at the next time step that then impacts the simulated turbulence and vertical mixing. Use of the PBL depth in this calculation has been done by several previous studies (e.g. Troen and Mahrt, 1986, Ballard et al., 1991, Mahrt and Vickers, 2003). This study seeks to understand the effect of changing the PBL depth definition used within the GEOS-5 AGCM to estimate the turbulent length scale and the impact on the emission, loss, and transport processes of atmospheric trace gases and aerosols. Section 2 describes the modeling system, PBL depth definitions, numerical experiments, and the validation datasets. Section 3 details the impacts of PBL depth definition on the simulated climate. The impact on tracer concentrations and transport are examined in more detail in Sect. 4. The final section contains the conclusions.

ACPD
14, 31627–31674, 2014

2 Experiment design

2.1 GEOS-5 model description

The GEOS-5 model is a comprehensive model used in different configurations for simulations of atmospheric dynamics and chemistry; atmospheric data assimilation operational analyses and reanalyses; and seasonal forecasting when coupled to an ocean model (Rienecker et al., 2008; Molod et al., 2012). The cubed sphere dynamical core is based on Putman and Lin (2007). Grid scale moist processes are described in Bacmeister et al. (2006) and Molod et al. (2012) and employ a modified version of relaxed Arakawa–Schubert convective parameterization (Moorthi and Suarez, 1992). The radiation schemes are described by Chou and Suarez (1999, shortwave) and Chou et al. (2001, longwave). The land surface model is the Catchment Land Surface Model (Koster et al., 2000), and the surface layer turbulence is from Helfand and Schubert (1995). Seventy-two vertical layers transition from terrain following near the surface to pure pressure levels above 180 hPa.

The GEOS-5 turbulence parameterization uses the non-local scheme of Lock et al. (2000) in conjunction with the Richardson number based scheme of Louis et al. (1982). The Lock scheme represents non-local mixing in unstable layers and computes the characteristics of rising or descending parcels of air resulting from surface heating and cloud top cooling of boundary layer clouds. The GEOS-5 implementation includes moist heating in the calculation of buoyancy and a shear-dependent entrainment in the unstable surface parcel calculations. This scheme can treat both clear and cloudy layers and the turbulent eddy diffusion coefficients are computed using a prescribed vertical structure based on the height of the surface or radiative parcels.

The Louis scheme computes eddy diffusion coefficients using Richardson number based stability functions for stable and unstable layers and is a first order, local scheme. This scheme requires the specification of a turbulent length scale, which is formulated using a Blackadar (1962) style interpolation between the height above the surface and a vertical scale based on the PBL height from the previous time step. Although many

ACPD
14, 31627–31674, 2014

AGCMs specify the length scale a priori to a constant global value (e.g. Sandu et al., 2013), the GEOS-5 formulation estimates this scale using the PBL depth diagnosed from the atmospheric profile from the previous model time step, adding "memory" and a dependence on the atmospheric state to the turbulence parameterization. This study modifies the PBL depth definition used within the Louis scheme turbulent length scale calculation and examines the model response.

2.2 GEOS-5 trace gas and aerosol emissions

The GEOS-5 AGCM includes a prognostic aerosol module based on the Goddard Chemistry, Aerosol, Radiation, and Transport (GOCART; Chin et al., 2002; Colarco et al., 2014). In this configuration, GEOS-5 simulates emission, transport, and loss of dust, sea salt, black carbon, organic carbon, and aerosols. The aerosol species are independent of one another. Aerosol loss processes depend on meteorological conditions such as wind and precipitation and the vertical distribution. The model also estimates wet and dry deposition and gravitational settling.

Dust and sea salt emissions depend on GEOS-5 wind speeds near the surface and, as a result, are likely to be particularly sensitive to changes in the model's treatment of turbulent mixing. Dust emissions are based on those of Ginoux et al. (2001) as modified by Chin et al. (2003). The emissions depend on wind speed, particle size, and surface wetness and the location of dust emissions are topographic depression areas with bare soil surfaces (Chin et al., 2003). Dust optical properties are prescribed based on data from the Aerosol Robotic Network (AERONET) (Holben et al., 1998) across the visible spectrum merged with the OPAC (Optical Properties of Aerosols and Clouds) dataset in the longwave (Randles et al., 2013). Sea salt emissions are computed as a function of sea salt particle radius and frictional velocity based on Gong (2003).

GEOS-5 also simulates emission and transport of a number of trace gases including CO and CO_2, which are evaluated in this study. Prescribed land and ocean CO_2 fluxes were computed as part of NASA's Carbon Monitoring System project and are described in detail in Ott et al. (2014). Three hourly net ecosystem production (NEP)

ACPD
14, 31627–31674, 2014

of CO_2 is computed by the Carnegie-Ames-Stanford Approach – Global Fire Emissions Database, version 3 (CASA-GFED3) biogeochemical model (Potter et al., 1993; Randerson et al., 1996). GFED3 biomass burning emissions are based on satellite estimates of area burned, fire activity, and plant productivity from the MODerate resolution Imaging Spectroradiometer (MODIS) (van der Werf et al., 2010). Ocean CO_2 fluxes are computed as a function of sea surface temperature, surface salinity, and partial pressure of CO_2 computed by the NASA Ocean Biogeochemical Model (Gregg, 2000, 2002; Gregg et al., 2003; Gregg and Casey, 2007) and 10 m wind speed and atmospheric CO_2 from the GEOS-5 AGCM. Fossil fuel emissions are from the Carbon Dioxide Information Analysis Center (CDIAC) computed using the procedure described by Marland and Rotty (1984; Marland et al., 2008).

Carbon monoxide (CO) emissions follow those of Duncan et al. (2007) and Duncan and Logan (2008). The Global Modeling Initiative (GMI) chemistry and transport model simulations were used to calculate methane and hydroxyl climatologies to estimate chemical production and loss in a computationally efficient manner. Biofuel emissions of CO are from Yevich and Logan (2003) and biomass burning estimates are from the daily Quick Fire Emission Database (Darmenov and da Silva, 2014).

2.3 PBL depth definitions

McGrath-Spangler and Molod (2014) evaluated various PBL depth definitions diagnostically, but the analysis did not include any PBL depth feedback on the turbulence length scale and therefore on the simulated climate. The present analysis examines the impact of three of those PBL depth definitions (summarized in Table 1) on tracer transport through their use in calculating the turbulent length scale. In this way, the different PBL depths are able to affect the climate and tracer transport within the model.

The first definition evaluated here is the method used to estimate the PBL depth in MERRA (Modern–Era Retrospective Analysis for Research and Applications) and MERRA2 (Method 1 from McGrath-Spangler and Molod, 2014). This method evaluates the vertical profile of the eddy diffusion coefficient of heat (K_h). The PBL height is

ACPD
14, 31627–31674, 2014

estimated as the height of the model level below where K_h falls below a threshold value of $2\,m^2\,s^{-1}$.

The second method (Method 2 of McGrath-Spangler and Molod, 2014) is also based on the vertical profile of K_h, but uses a variable threshold equal to 10 % of the column maximum K_h and linearly interpolates between model levels. The variable threshold was chosen because of its state dependence and therefore its spatiotemporal variability.

The final method evaluated here is Method 4 of McGrath-Spangler and Molod (2014) and depends on a bulk Richardson number as described by Seidel et al. (2012). This definition is suitable for both convective and stable boundary layers and was shown by McGrath-Spangler and Molod (2014) to produce a more realistic diurnal cycle of PBL depth over many land areas. The bulk Richardson number (Ri_b) is given by:

$$Ri_b(z) = \frac{\left(\frac{g}{\theta_{vs}}\right)(\theta_{vz} - \theta_{vs})(z - z_s)}{u_z^2 + v_z^2}$$

where g is gravitational acceleration, θ_v is the virtual potential temperature, u and v are the horizontal wind components, and z is height above the ground. The subscript s denotes the surface and the bulk Richardson number is evaluated between the surface and successively higher levels. Surface winds are assumed negligible. The PBL top is found by linearly interpolating between model levels using a critical value of 0.25.

2.4 Experimental configuration

In order to isolate the climate response to PBL depth from internal model variability, model ensembles are run with ten simulations for each of the three PBL depth definitions from January 2009 through February 2010. Ensemble means are used for the comparisons here. Each ensemble is initialized using MERRA reanalysis data from a different day (between 15 November and 15 December 2008) although all simulations begin on 30 November 2008. The first month of each simulation is disregarded

ACPD
14, 31627–31674, 2014

as a spin up period and is not used in the analysis. The simulations are on a cubed sphere grid with approximately 2 degree horizontal resolution. While SSTs and emissions datasets from 2008 are used, all simulations are run in GEOS-5 "climate mode" with no constraint by meteorological reanalyses.

2.5 Validation data

The ensemble means of the simulations using the different PBL height definitions are compared here to various observational datasets in a climatological sense to provide validation of meteorological and tracer fields. The MERRA reanalysis used a three-dimensional variational data assimilation (3DVAR) analysis algorithm to incorporate observations from conventional platforms such as weather stations, balloons, aircraft, ships, and buoys as well as satellite radiances from multiple platforms (e.g. TRMM, AIRS, QuikScat, AMSU-A/B) (Rienecker et al., 2011). An incremental analysis update (IAU, Bloom et al., 1996) is implemented in MERRA to eliminate shocks to the model system caused by large, infrequent updates.

Aerosol optical thickness (AOT) data are available from the Moderate-Resolution Imaging Spectroradiometer (MODIS, Remer et al., 2005) and the Multiangle Imaging Spectroradiometer (MISR, Kahn et al., 2010) instruments for comparison with the free-running model. The MODIS instruments were launched aboard both the Terra and Aqua satellites while MISR was launched on the Terra satellite only.

The MERRA Aerosol (MERRAero, Kishcha et al., 2014) reanalysis uses MERRA estimated meteorology, assimilates MODIS AOT data from the Terra and Aqua satellites, and provides data on dust, sea salt, sulfates, and black and organic carbon. MERRAero data begin in 2002 and provide global aerosol concentrations at 3 hourly intervals.

The Measurement of Pollution in the Troposphere (MOPITT) instrument, also onboard the Terra satellite, is a mission designed to measure carbon monoxide (CO) from space in order to quantify tropospheric pollution. It uses a nadir IR correlation radiometer with a field of view of 22 km × 22 km (Drummond and Mand, 1996). This study uses the TIR/NIR version 5 data.

ACPD
14, 31627–31674, 2014

The Atmospheric CO_2 Observations from Space (ACOS version 3.4) project estimates column CO_2 using observations from the Greenhouse Gases Observing Satellite (GOSAT). Launched in January 2009, GOSAT's onboard instrument, the Thermal And Near-infrared Sensor for carbon Observation Fourier Transform Spectrometer (TANSO-FTS), measures spectra of reflected sunlight in order to make this estimate (Yokota et al., 2004; Hamazaki et al., 2005). Details of the ACOS retrieval can be found in Wunch et al. (2011), O'Dell et al. (2012), and Crisp et al. (2012).

The International Satellite Cloud Climatology Project (ISCCP) dataset contains a global climatology of cloud properties derived from infrared and visible radiances observed by both geostationary and polar-orbiting satellites in the constellation of weather satellites (Rossow and Schiffer, 1991, 1999). The goal of this project was to improve the understanding of the effects of clouds on climate, the radiation budget, and the global hydrological cycle. Data are available from July 1983 through June 2008.

3 Impact on model climate

Observational and modeling studies have found that different PBL depth estimation methods can produce depth estimates that vary by hundreds of meters, even when analyzing the same atmospheric profile (e.g. Seidel et al., 2010; McGrath-Spangler and Molod, 2014). In this study, the methods used depend on different atmospheric variables with the Bulk *Ri* method dependent on vertical profiles of temperature and wind speed and the K_h methods dependent on vertical profiles of turbulent eddy diffusion coefficients. McGrath-Spangler and Molod (2014) found that over land these differences result in lower nocturnal PBL depth estimates using the Bulk *Ri* method due to persistent turbulence and elevated K_h aloft throughout the diurnal cycle, resulting in deeper PBL estimates using Methods 1 and 2. The methodological differences resulted in differences in the climatological mean estimates.

These differences in PBL depth have consequences for land–atmosphere interactions and for radiation. Shallower PBLs result in a shallower turbulent layer so that

ACPD
14, 31627–31674, 2014

surface fluxes are not mixed as high vertically and boundary layer top entrainment occurs at a lower height. Lower boundary layer top entrainment results in entrained air generally being moister and with a lower potential temperature than if the entrainment occurred higher. Beljaars and Betts (1992) found in their study that the proper representation of entrainment is essential to correctly simulate near surface atmospheric conditions with too low PBL depth estimates resulting in a near surface atmosphere that is too cool and to moist. PBL depth differences thus change the atmospheric conditions to which the surface responds through differences in the temperature and humidity gradients between the atmosphere and the surface (McGrath-Spangler et al., 2009; McGrath-Spangler and Denning, 2010). Changes to the surface sensible and latent heat fluxes can result in modifications to the moisture and energy available at cloud layer and produce either increases or decreases in cloud amount. This, in turn, produces changes in cloud albedo and the vertical redistribution of short and longwave radiation.

Seasonal mean PBL depth (Fig. 1) differences among the three ensemble means are generally similar to the differences described in McGrath-Spangler and Molod (2014). Over land, Method 1 (K_h: 2) estimates the greatest PBL depths in both seasons while Method 3 (Bulk *Ri*) estimates lower depths due largely to a better representation of the shallow nighttime PBL. There are a few coastal exceptions to Method 3 (Bulk *Ri*) estimating shallower PBLs during June–August (JJA) along the horn of Africa and over the Indian subcontinent and in December–February (DJF) over the British Isles where the Bulk *Ri* method estimates greater depths. Over the Southern Ocean, the Bulk *Ri* method (Method 3) generally estimates the deepest PBLs, indicative of a shallow turbulence layer defined by K_h relative to the unstable layer as defined by the bulk Richardson number.

Over much of Asia, the tropics, and western and southern North America, Method 1 (K_h: 2) estimates a greater PBL depth than Method 2 (K_h: 10 %) during JJA. This implies that in these areas, 10 % of the column maximum K_h is greater than the 2 $m^2 s^{-1}$ threshold used by Method 1 and there is relatively strong turbulence. During DJF,

ACPD
14, 31627–31674, 2014

Method 2 estimates deeper PBLs than does Method 1 over much of the United States, the Saharan Desert and Sahel, and parts of Asia, indicating weaker turbulence, consistent with greater atmospheric stability and suppressed turbulence over land during the colder months. Over water, in most areas, Method 1 produces deeper PBLs than does Method 2. However, since they both depend on the turbulent eddy diffusion coefficient, in general, Methods 1 and 2 are more similar to each other than they are to Method 3. Since these methods are so similar, the remainder of this discussion concentrates on differences between Methods 2 and 3.

The turbulent eddy diffusion coefficient is dependent on PBL depth so changes in its estimation will produce changes in K_h. Under unstable conditions, as the PBL depth increases, the Louis scheme length scale used in the calculation of the turbulent eddy diffusion coefficient for this scheme also increases. Since the total eddy diffusion coefficient is a combination of those computed by the Louis and Lock schemes, an increase in the PBL depth can lead to an increase in K_h and the turbulent mixing.

The largest K_h (Fig. 2) differences in the lower troposphere occur over the Southern Hemisphere oceans where Method 3 (Bulk *Ri*) estimates deeper PBLs. Large differences also occur along the Atlantic and Pacific Oceans' storm tracks during DJF. Midday PBL depths over land (not shown) estimated by the three methods are similar, producing small turbulent length scale differences and a small impact on turbulence. At night, PBL depth differences are much larger over land, producing correspondingly different turbulent length scales among the simulations. However, nighttime conditions are generally stable and the turbulent length scale is unused in the calculation of turbulence so differences could be related to feedbacks between the large-scale meteorology and the turbulence. Only small regions over the United States Great Lakes region and north of the Caspian Sea during JJA have significant seasonal mean differences in K_h over land.

These changes in turbulence lead to changes in the simulated climate of the model. Figure 3 shows the impact on the mean meridional circulation. Significant differences are present between the two simulations in the estimation of the Hadley cell during

ACPD
14, 31627–31674, 2014

DJF and JJA. For experiment 3 (Bulk *Ri*), the strength of the inner core of the Hadley cell is increased in the DJF and JJA seasons. A weakening of the northern edge of the Hadley circulation is present in DJF, indicating less subsidence around 30° N. During the transition seasons of March–May (MAM) and September–November (SON), the differences between the Bulk *Ri* and K_h: 10 % experiments are smaller than during JJA and DJF and the area of significant differences is less.

Changes in the turbulence and mean circulation result in a redistribution of atmospheric mass that can be seen as changes in the surface pressure (Fig. 4). Seasonal mean pressure changes mostly occur in small regions over the Southern Ocean with a magnitude on the order of 1 to 2 hPa. The increased pressure over the Southern Ocean in experiment 3 (Bulk *Ri*) disagrees with MERRA more so than the surface pressure in experiment 2 (K_h: 10 %). In regions where the surface pressure is decreased in experiment 3 relative to experiment 2 over the Southern Ocean, the surface pressure agrees better with MERRA (not shown). These differences produce changes to the pressure gradient force and are associated with differences in the near surface wind.

Figure 5 compares the 10 m wind speed estimated using the Bulk *Ri* method (Method 3) and the K_h: 10 % method (Method 2) and the MERRA reanalysis estimate. Significant differences between the simulations occur over the Southern Ocean south of the African continent during JJA and southwest of South America in both seasons. During JJA, this increase in wind speed for experiment 3 is a result of a deeper low pressure over Antarctica from 60° W to the dateline and increased pressure over the southern Pacific and Indian Oceans from approximately 30 to 60° S. These changes lead to an improved estimate of the wind speed relative to MERRA. During DJF, the change in pressure gradient is reversed, leading to a decrease in the wind speed and degradation of the estimate relative to MERRA.

During JJA, experiment 3 (Bulk *Ri*) has increased easterly winds over the Atlantic Ocean relative to experiment 2 (K_h: 10 %) associated with an increase in the Atlantic subtropical high. Experiment 2's wind speed in this region is greater than in MERRA and the increase in experiment 3 exacerbates the disagreement. There is also an

ACPD
14, 31627–31674, 2014

increase in wind speed over the Pacific Ocean associated with decreased pressure over the Asian continent in experiment 3, which is an improvement when compared to MERRA relative to experiment 2.

In addition to the winds, near surface temperature is sensitive to changes in the PBL depth estimate used to calculate the turbulent length scale. Figure 6 shows the 2 m temperature differences between experiments 2 and 3 (Bulk *Ri* and K_h: 10 %) relative to the temperature estimated by MERRA. Significant temperature differences are present over the tropical land areas of the Amazon, Congo, and the maritime continent with experiment 3 simulating cooler temperatures. These are the regions associated with a lower midday PBL depth diagnosed by the bulk Richardson number method relative to the turbulent eddy diffusion coefficient methods in McGrath-Spangler and Molod (2014).

During DJF, the Bulk *Ri* experiment simulates cooler temperatures in the Pacific Northwest of the United States and at high northern latitudes. These changes are associated with less surface absorbed longwave radiation. Over most land areas, the free-running GEOS-5 AGCM overestimates the temperature relative to MERRA (Molod et al., 2012) so a temperature decrease is generally an improvement.

Changes in near surface specific humidity (Fig. 7) also result from changes to the PBL depth estimate used in the turbulent length scale calculations; most regions experience lower humidity levels in experiment 3 (Bulk *Ri*). The Great Lakes region of the United States, during JJA, experiences a larger diurnal cycle of the PBL depth using Method 3 (Bulk *Ri*) than when using Method 2 (K_h: 10 % experiment), due to lower nocturnal PBL depths combined with greater daytime depths. This is associated with warmer temperatures and lower humidity. Specific humidity differences in this region are on the order of 1 g kg^{-1} or about 10 % of the mean value. These changes are more similar to MERRA.

Spain, southern Africa, and southeastern Asia (along the eastern edge of the Bay of Bengal) have higher estimated specific humidity in experiment 3 (Bulk *Ri*), associated with decreased near surface temperatures. Significant differences in these regions are

ACPD
14, 31627–31674, 2014

on the order of 0.8 g kg^{-1} over Spain (~ 12 % of the mean total) and Africa (~ 18 % of the mean total) and 1.2 g kg^{-1} over Asia (~ 8 % of the mean total). In these regions there is also increased soil moisture and a shift in the Bowen ratio (not shown) with more latent heat flux in the Bulk *Ri* experiment. Over Spain and southern Africa, these changes are less similar to the specific humidity estimated by MERRA, but over south-eastern Asia, they are more similar.

Generally, experiment 3 (Bulk *Ri*) predicts more marine low level clouds than does experiment 2 (K_h: 10 %) (Fig. 8). Exceptions to this are along the equator off the west coast of South America in both seasons and Africa in JJA. The overall increase in low level clouds is associated with an increase in latent heat flux over the oceans due, in part, to the increase in the low level wind speeds. The increase is particularly evident south of 30° S, over the subtropical Atlantic, and off the west coast of North America during DJF and the west coast of South America in both seasons. In comparison to the ISCCP climatology, experiment 3 better predicts cloud cover between 30° N and 30° S, but is worse in the extratropics. Exceptions to this are the regions of equatorial decrease in low level cloud cover off the west coasts of South America and Africa.

In summary, changes in PBL depth, specifically lower PBL depths over land due to lower nocturnal PBL depths and greater depths over oceans when using Method 3, lead to differences in turbulent mixing and subsequently to differences in the mean circulation. This redistribution of mass leads to changes in temperature, specific humidity, and wind velocity and consequently to changes in cloud cover.

4 Impact on tracer transport

Modifications to the model climate result in changes to trace gas and aerosol transport and concentrations. Some species are directly dependent on the model climate for their emissions and all tracers are subject to changes in turbulent mixing and horizontal advection. Atmospheric dust concentrations are particularly sensitive to PBL depth estimates because their emission is sensitive to wind speed, and the height to which

ACPD
14, 31627–31674, 2014

they are mixed vertically in the atmosphere depends on the turbulence determined, in part, by the PBL depth. This is significant for deposition and settling of the dust particles. Another consequence for the chemical composition of the atmosphere is that in the GEOS-5 AGCM, the PBL depth determines the depth to which biomass burning emissions are homogeneously emitted, meaning that, over fires, shallower PBLs result in a higher near surface concentration of chemical species like carbon monoxide. This has implications for chemical processes dependent on the availability of these species.

Figure 9 shows aerosol optical thickness from the MODIS and MISR instruments compared to that simulated by the model using the three PBL depth definitions. Qualitatively, the results are similar among the model simulations and the observations. The highest AOT is present over the Saharan Desert and the dust outflow region over the Atlantic Ocean. Other maxima exist near biomass burning and industrial areas. The lowest simulated AOT occurs over the high latitudes, which the satellites do not observe. The model estimates a higher AOT than do the satellite observations, due partially to the inability of the satellites to observe all locations. Mean AOT values observed by MODIS/Terra, MODIS/Aqua, and MISR are 0.1277, 0.1339, and 0.1808 respectively. MISR detects a higher AOT value because it is able to sense aerosols over reflective surfaces and therefore is able to observe over the Saharan Desert. The model simulations estimate AOT values of 0.1985, 0.1943, and 0.2153 for the K_h: 2, K_h: 10 % and Bulk *Ri* experiments respectively. Overall, the model is able to represent the observed AOT reasonably well.

Due to its dependence on surface winds, the emission of Saharan Desert dust (Fig. 10) is increased in experiment 3 (Bulk *Ri*) during JJA, consistent with the increased wind speed in this experiment. Figure 11 shows the global impact of these dust emission changes on the total column dust concentration. Globally, percentage differences range from zero to 50 %. The largest significant changes are over the Saharan Desert and downwind over the Atlantic Ocean. Increased Saharan dust emissions produce an increase in atmospheric dust that is then transported downwind, mostly between 800 and 500 hPa (Fig. 12), to the Caribbean and North America, increas-

ACPD
14, 31627–31674, 2014

ing column concentrations there. Although column concentrations are increased in the western Atlantic, surface concentrations actually decrease in experiment 3. Increased dust aloft increases the shortwave radiation temperature tendency due to aerosols producing warmer temperatures there and shading the lower atmosphere (and decreasing the shortwave radiation temperature tendency due to aerosols) thus producing cooling near the surface (not shown). This creates an increase in lower tropospheric stability and acts to reduce the mixing of dust downward.

During DJF, the opposite impact is seen over the Saharan Desert. Surface winds decrease in experiment 3 (Bulk *Ri*), leading to a decrease in desert dust emissions there (Fig. 10). This, in turn, leads to a decrease in the column dust concentrations over northwestern Africa and downwind over the subtropical Atlantic Ocean. The impact does not extend as far downwind during DJF as it does during JJA, due in part to the more southerly location of the easterly jet. Over the Arabian Peninsula, experiment 3 (Bulk *Ri*) winds are greater than in experiment 2 (K_h: 10 %), leading to increased desert dust emissions and increased column concentrations that extend to the northwest into central Asia.

In both seasons, the free-running model overestimates column dust concentrations over northern Africa and downwind across the Atlantic compared to MERRAero. Therefore, the reduction in column dust is an improvement over northwestern Africa in DJF and the increase during JJA is a degradation. This is despite an indication from McGrath-Spangler and Molod (2014) that the bulk Richardson number based definition better represents the nocturnal PBL depth over the Sahara than the scalar diffusivity based ones.

The amount of sea salt aerosol in the atmospheric column (Fig. 13) is generally greater in experiment 3 (Bulk *Ri*) due to an overall increase in wind speed over the oceans used to estimate sea salt emission into the atmosphere. Although experiment 3 is able to produce a similar pattern as MERRAero, the free-running model overestimates the sea salt concentration and experiment 2 performs better.

ACPD
14, 31627–31674, 2014

In the GEOS-5 AGCM, biomass burning emissions are instantaneously mixed vertically throughout the PBL so surface concentrations of CO from fires are inversely related to the depth of the PBL. Surface CO patterns in the model and MOPITT observations are generally consistent (Fig. 14). In general, biomass burning emissions over Africa are further north in DJF than in JJA, and the seasonality is properly captured in all model simulations. Surface CO concentrations over the industrial cities of China increase during DJF (MOPITT estimates about 350 ppb) relative to JJA (MOPITT estimates about 250 ppb), associated with lower tropospheric stability and lower PBL depths.

During JJA, the largest CO concentration differences between experiments 2 and 3 (Bulk Ri and K_h: 10 %) are present over the biomass burning regions of Africa (MOPITT estimates about 100–300 ppb), especially over Ethiopia and Sudan (decreased concentrations in experiment 3) and over South Africa (increased in experiment 3). Over South Africa, the PBL depth estimated by Method 3 is about 1 km lower than in the scalar diffusion coefficient method, concentrating CO near the surface there. The decrease over Ethiopia, Sudan, and the Indian subcontinent in experiment 3 is due to an increased daytime PBL depth diluting CO emissions and leading to lowered surface concentrations. The surface CO differences over Africa are an improvement relative to MOPITT observations, however the decrease over the Indian subcontinent is not.

During DJF, surface CO differences over Africa are much smaller and the area with significant differences is reduced. However, there are significant decreases in surface CO over eastern China and the Great Lakes region of the United States in experiment 3. These regions have bulk Richardson number estimated daytime PBL depths that are greater than those in the other experiment and the associated increase in vertical mixing leads to a decrease in surface CO concentrations. Over China, the decreased surface CO compares better to the MOPITT estimated concentrations. Differences in CO extend vertically through the atmosphere, leading to differences at 500 hPa of up to 18 ppb (not shown). These free-tropospheric differences affect the horizontal transport of CO over long distances.

ACPD
14, 31627–31674, 2014

Figure 15 shows the column CO_2 differences among experiments 2 and 3 (K_h:10 % and Bulk *Ri*) and the ACOS retrieval from GOSAT. In general, the model overestimates column CO_2 over extratropical land compared to the observations. However, time mean differences between experiments 2 and 3 are only significant over small regions in the tropics where there are no ACOS retrievals. In most regions, the differences do not exceed the internal model variability.

Figure 16 shows the impact of PBL depth definition on the surface CO_2 concentration. In JJA, there are large regions of CO_2 differences over the Indian and Pacific Oceans and over the Caribbean Sea, where experiment 3 simulated CO_2 concentrations about 1 ppm lower than experiment 2. This occurs in regions with increased PBL depth, where oceanic emissions of CO_2 are diluted thereby decreasing the surface concentration. Also during JJA, a seasonal mean increase in CO_2 occurs over central South America associated with nocturnal PBLs in experiment 3 a kilometer lower than in experiment 2, concentrating nighttime CO_2 respiration emissions and increasing surface concentrations there.

The largest seasonal mean CO_2 differences occur during DJF. Over the western United States and Canada, experiment 3 (Bulk *Ri*) estimates CO_2 concentrations about 3 ppm greater than in experiment 2 (K_h: 10 %). In this region, experiment 3 estimates shallower PBLs throughout the diurnal cycle, producing a concentration of CO_2 emissions and higher concentrations there.

Regions with persistent and significant surface CO_2 biases due to PBL depth changes are small. This is partly because synoptic variability can produce CO_2 variations on the order of 10–20 ppm that are averaged out in the time mean (Parazoo et al., 2008). Figure 17 shows an example of surface CO_2 differences between experiments 2 and 3 at specific times during JJA and DJF. On these smaller time scales, surface CO_2 differences are much larger than in the time mean, on the order of 10 ppm, and these differences are significant globally. This is especially true during DJF at mid and high northern latitudes where differences are often on the order of 15 ppm and are advected along with synoptic storms. Figure 17 also shows the SD of surface CO_2 differences

ACPD
14, 31627–31674, 2014

for July and January. The greatest variability is present during January over high latitude land with SDs exceeding 7 ppm over parts of Asia. Generally, variability is high over land in both seasons. This has implications for inversion studies that often assume perfect transport. Uncertainty in estimated CO_2 concentrations may be incorrectly attributed to surface fluxes rather than errors in assumed vertical transport.

5 Conclusions

Weather, climate, and tracer transport and concentrations are sensitive to PBL processes. One way to quantify these processes is with the depth of the PBL. However, multiple PBL depth definitions exist and these estimated depths can vary substantially, even if defined using the same atmospheric profile. In the GEOS-5 AGCM, the PBL depth is used to calculate the turbulent length scale that is used to estimate the model turbulence at the next time step, making it important to properly estimate this depth.

This study analyzed three PBL depth definitions. Two are based on the turbulent eddy diffusion coefficient and use threshold values of $2\,m^2\,s^{-1}$ (K_h: 2, Method 1) and 10 % of the column maximum (K_h: 10 %, Method 2). The third method uses the bulk Richardson number definition (Bulk *Ri*, Method 3) described by Seidel et al. (2012). Ten ensemble members were run for each of these definitions and comparisons were made between the ensemble means. The Bulk *Ri* ensemble (experiment 3) generally estimated a lower PBL depth over land due to lower nocturnal PBL depths. This is consistent with the result of McGrath-Spangler and Molod (2014) who diagnosed several PBL depths from a single atmosphere using various definitions.

The different PBL depth definitions, when used to inform the turbulent length scale in the model, resulted in a large-scale climatic response. The response was characterized by a redistribution of atmospheric mass and subsequent changes in winds. During JJA in experiment 3, increased wind speed over the Saharan Desert resulted in increased dust emissions and column dust concentrations over the desert and downwind over the Atlantic Ocean. The near surface temperature and specific humidity were also modified

ACPD
14, 31627–31674, 2014

in experiment 3 resulting in improvements in temperature over much of the land surface and in specific humidity over the Great Lakes region of the United States and southeast Asia. Degradations occurred over Spain and southern Africa.

In addition to dust, other tracers were impacted by changes in the PBL depth definition. In experiment 3, increased PBL depth during JJA over equatorial Africa and the Indian subcontinent and during DJF over eastern China and the Great Lakes region of the United States led to a dilution of CO from biomass burning and lower concentrations that constituted an improvement relative to experiment 2 when compared to MOPITT observations.

Differences between the simulations' CO_2 estimates were most significant near the surface and in instantaneous fields. Time mean differences are generally not significant and small (on the order of a few ppm), differences at shorter timescales are globally significant and large (on the order of 10 ppm), especially during DJF at high northern latitudes when synoptic systems are most prevalent.

PBL depth differences between the model simulations occur due to methodological differences and inconsistencies between the depth of the turbulent layer as defined by the turbulent eddy diffusion coefficient and the unstable layer as defined by the bulk Richardson number used here. These differences have consequences for land–atmosphere interactions, radiation, and atmospheric chemistry because of impacts on the vertical extent of turbulent mixing. It is therefore important to carefully consider the impact on model climate and tracer concentrations when modifying the simulated PBL depth in GEOS-5. While the Bulk *Ri* experiment generally predicts a more reasonable diurnal cycle of PBL depth, other aspects of the simulation are not universally improved.

Only one year is simulated and the free-running AGCM does not simulate any specific weather event, limiting direct comparisons to observations. Future research should include long-term climatological simulations that estimate the impact of PBL depth on GEOS-5 model climate and further isolate the climatic response to PBL depth definition from internal model variability. The GEOS-5 AGCM is sensitive to the estimated PBL depth and the definition used can affect model climate and the estimated distribu-

ACPD
14, 31627–31674, 2014

tion of greenhouse gases and atmospheric aerosols relevant for climate and air quality research.

Acknowledgements. The MERRA data are produced by the NASA Global Modeling and Assimilation Office and disseminated by the GES DISC. The ACOS data were produced by the ACOS/OCO-2 project at the Jet Propulsion Laboratory, California Institute of Technology using spectra data acquired by the GOSAT Project. We would like to acknowledge the NASA Langley Research Center Atmospheric Science Data Center for disseminating the MOPITT and ISCCP data, the Goddard DAAC and MODIS software development and support teams for providing the MODIS data, and the MISR retrieval team. Computing was supported by the NASA Center for Climate Simulation. The research was supported by National Aeronautics and Space Administration grant NNG11HP16A.

References

Bacmeister, J. T., Suarez, M. J., and Robertson, F. R.: Rain reevaporation, boundary layer-convection interactions, and Pacific rainfall patterns in an AGCM, J. Atmos. Sci., 63, 3383–3403, doi:10.1175/jas3791.1, 2006.

Baker, D. F., Law, R. M., Gurney, K. R., Rayner, P., Peylin, P., Denning, A. S., Bousquet, P., Bruhwiler, L., Chen, Y.-H., Ciais, P., Fung, I. Y., Heimann, M., John, J., Maki, T., Maksyutov, S., Masaarie, K., Prather, M., Pak, B., Taguchi, S., and Zhu, Z.: TransCom 3 inversion intercomparison: impact of transport model errors on the interannual variability of regional CO_2 fluxes, 1988–2003, Global Biogeochem. Cy., 20, GB1002, doi:10.1029/2004GB002439, 2006.

Balkanski, Y., Schulz, M., Claquin, T., and Guibert, S.: Reevaluation of Mineral aerosol radiative forcings suggests a better agreement with satellite and AERONET data, Atmos. Chem. Phys., 7, 81–95, doi:10.5194/acp-7-81-2007, 2007.

Ballard, S. P., Golding, B. W., and Smith, R. N. B.: Mesoscale model experimental forecasts of the Haar of northeast Scotland, Mon. Weather Rev., 119, 2107–2123, doi:10.1175/1520-0493(1991)119<2107:MMEFOT>2.0.CO;2, 1991.

Beljaars, A. C. M. and Betts, A. K.: Validation of the boundary layer representation in the ECMWF model, in: ECMWF Seminar Proceedings, Reading, UK, Validation of models over Europe, Vol II, 7–11 September 1992, 159–195: available at: http://old.ecmwf.int/

ACPD
14, 31627–31674, 2014

publications/library/ecpublications/_pdf/seminar/1992/validation2_beljaars.pdf (last access: 24 October 2014), 1992.
Blackadar, A. K.: The vertical distribution of wind and turbulent exchange in a neutral atmosphere, J. Geophys. Res., 67, 3095–3102, doi:10.1029/JZ067i008p03095, 1962.
Bloom, S., Takacs, L., Da Silva, A., and Ledvina, D: Data assimilation using incremental analysis updates, Mon. Weather Rev., 124, 1256–1271, 1996.
Chin, M., Ginoux, P., Kinne, S., Torres, O., Holben, B. N., Duncan, B. N., Martin, R. V., Logan, J. A., Higurashi, A., and Nakajima, T.: Tropospheric aerosol optical thickness from the GOCART model and comparisons with satellite and sunphotometer measurements, J. Atmos. Sci., 59, 461–483, doi:10.1175/1520-0469(2002)059<0461:TAOTFT>2.0.CO;2, 2002.
Chin, M., Ginoux, P., Lucchesi, R., Huebert, B., Weber, R., Anderson, T., Masonis, S., Blomquist, B., Bandy, A., and Thornton, D.: A global aerosol model forecast for the ACE-Asia field experiment, J. Geophys. Res., 108, 8654, doi:10.1029/2003JD003642, 2003.
Chou, M.-D. and Suarez, M. J.: A solar radiation parameterization for atmospheric studies, Technical Report Series on Global Modeling and Data Assimilation, 40 pp.: available at: http://gmao.gsfc.nasa.gov/pubs/docs/Chou136.pdf (last access 4 March 2014), 1999.
Chou, M.-D., Suarez, M. J., Liang, X.-Z., and Yan, M. M.-H.: A thermal infrared radiation parameterization for atmospheric studies, Technical Report Series on Global Modeling and Data Assimilation, 56 pp.: available at: http://gmao.gsfc.nasa.gov/pubs/tm/docs/Chou137.pdf (last access 4 March 2014), 2001.
Colarco, P. R., Nowottnick, E. P., Randles, C. A., Yi, B., Yang, P., Kim, K.-M., Smith, J. A., and Bardeen, C. G.: Impact of radiatively interactive dust aerosols in the NASA GEOS-5 climate model: sensitivity to dust particle shape and refractive index, J. Geophys. Res.-Atmos., 119, 753–786, doi:10.1002/2013JD020046, 2014.
Conway, T. J., Tans, P. P., Waterman, L. S., Thoning, K. W., Kitzis, D. R., Masarie, K. A., and Zhang, N: Evidence for interannual variability of the carbon cycle from the National Oceanic and Atmospheric Administration/Climate Monitoring and Diagnostics Laboratory Global Air Sampling Network, J. Geophys. Res., 99, 22831–22855, doi:10.1029/94JD01951, 1994.
Crisp, D., Fisher, B. M., O'Dell, C., Frankenberg, C., Basilio, R., Bösch, H., Brown, L. R., Castano, R., Connor, B., Deutscher, N. M., Eldering, A., Griffith, D., Gunson, M., Kuze, A., Mandrake, L., McDuffie, J., Messerschmidt, J., Miller, C. E., Morino, I., Natraj, V., Notholt, J., O'Brien, D. M., Oyafuso, F., Polonsky, I., Robinson, J., Salawitch, R., Sherlock, V., Smyth, M., Suto, H., Taylor, T. E., Thompson, D. R., Wennberg, P. O., Wunch, D., and Yung, Y. L.: The

ACPD
14, 31627–31674, 2014

ACOS CO_2 retrieval algorithm – Part II: Global XCO_2 data characterization, Atmos. Meas. Tech., 5, 687–707, doi:10.5194/amt-5-687-2012, 2012.
Darmenov, A. S. and da Silva, A.: The Quick Fire Emissions Dataset (QFED) – Documentation of versions 2.1, 2.2, and 2.4., Vol 35, Technical Report Series on Global Modeling and Data Assimilation, NASA/TM-2014-104606, edited by: Koster, R. D., in preparation, 2014.
Davis, K. J., Bakwin, P. S., Yi, C., Beger, B. W., Zhao, C., Teclaw, R. M., and Isebrands, J. G.: The annual cycles of CO_2 and H_2O exchange over a northern mixed forest as observed from a very tall tower, Glob. Change Biol., 9, 1278–1293, doi:10.1046/j.1365-2486.2003.00672.x, 2003.
Drummond, J. R. and Mand, G. S.: The Measurements of Pollution in the Troposphere (MOPITT) instrument: overall performance and calibration requirements, J. Atmos. Ocean. Tech., 13, 314–320, doi:10.1175/1520-0426(1996)013<0314:TMOPIT>2.0.CO;2, 1996.
Duncan, B. N., Logan, J. A., Bey, I., Megretskaia, I. A., Yantosca, R. M., Novelli, P. C., Jones, N. B., and Rinsland, C. P.: The global budget of CO, 1988–1997: source estimates and validation with a global model, J. Geophys. Res., 112, D22301, doi:10.1029/2007JD008459, 2007.
Duncan, B. N. and Logan, J. A.: Model analysis of the factors regulating the trends and variability of carbon monoxide between 1988 and 1997, Atmos. Chem. Phys., 8, 7389–7403, doi:10.5194/acp-8-7389-2008, 2008.
Fung, I. Y., Meyn, S. K., Tegen, I. Doney, S. C., John, J. G., and Bishop, J. K. B.: Iron supply and demand in the upper ocean, Global Biogeochem. Cy., 14, 281–295, doi:10.1029/1999GB900059, 2000. .
Gerbig, C., Lin, J. C., Wofsy, S. C., Dabe, B. C., Andrews, A. E., Stephens, B. B., Bakwin, P. S., and Grainger, C. A.: Toward constraining regional-scale fluxes of CO_2 with atmospheric observations over a continent: 1. Observed spatial variability from airborne platforms, J. Geophys. Res., 108, 4756, doi:10.1029/2002JD003018, 2003.
Ginoux, P., Chin, M., Tegen, I., Prospero, J., Holben, B., Dubovik, O., and Lin, S.-J.: Sources and global distributions of dust aerosols simulated with the GOCART model, J. Geophys. Res., 106, 20255–20273, doi:10.1029/2000JD000053, 2001.
Gong, S. L.: A parameterization of sea-salt aerosol source function for sub- and super-micron particles, Global Biogeochem. Cy., 17, 1097, doi:10.1029/2003GB002079, 2003.
Gregg, W. W.: A coupled ocean general circulation, biogeochemical, and radiative model of the global oceans: seasonal distributions of ocean chlorophyll and nutrients. NASA Technical

ACPD
14, 31627–31674, 2014

Memorandum 2000–209965, 33 pp., available at: http://ntrs.nasa.gov/archive/nasa/casi.ntrs.nasa.gov/20000112962.pdf (last access 11 April 2014), 2000.
Gregg, W. W.: Tracking the SeaWiFS record with a coupled physical/biogeochemical/radiative model of the global oceans, Deep-Sea Res. II, 49, 81–105, doi:10.1016/S0967-0645(01)00095-9, 2002.
Gregg, W. W. and Casey, N. W.: Modeling coccolithophores in the global oceans, Deep-Sea Res. II, 54, 447–477, doi:10.1016/j.dsr2.2006.12.007, 2007.
Gregg, W. W., Ginoux, P., Schopf, P. S., and Casey, N. W.: Phytoplankton and iron: validation of a global three-dimensional ocean biogeochemical model, Deep-Sea Res. II, 50, 3143–3169, doi:10.1016/j.dsr2.2003.07.013, 2003.
Gurney, K. R., Law, R. M., Denning, A. S., Rayner, P. J., Baker, D., Bousquet, P., Bruhwiler, L., Chen, Y.-H., Ciais, P., Fan, S., Fun, I. Y., Gloor, M., Heimann, M., Higuchi, K., John, J., Maki, T., Maksyutov, S., Masarie, K., Peylin, P., Prather, M., Pak, B. C., Randerson, J., Sarmiento, J., Taguchi, S., Takahaskhi, T., and Yuen, C.-W.: Towards robust regional estimates of CO_2 sources and sinks using atmospheric transport models, Nature, 415, 626–630, doi:10.1038/415626a, 2002.
Hamazaki, T., Kaneko, Y., Kuze, A., and Kondo, K.: Fourier transform spectrometer for greenhouse gases observing satellite (GOSAT), Proceedings of Enabling Sens. Platf. Technol. Spaceborne Remote Sens., SPIE 5659, 73–80, doi:10.1117/12.581198, 2005.
Helfand, H. M. and Schubert, S. D.: Climatology of the simulated great plains low-level jet and its contribution to the continental moisture budget of the United States, J. Climate, 8, 784–806, doi:10.1175/1520-0442(1995)008<0784:cotsgp>2.0.co;2, 1995.
Holben, B. N., Eck, T. F., Slutsker, I., Tanré, D., Buis. J. P., Setzer, A., Vermote, E., Reagan, J. A., Kaufman, Y. J., Nakajima, T., Lavenu, F., Jankowiak, I., and Smirnov, A.: AERONET – A federated instrument network and data archive for aerosol characterization, Remote Sens. Environ., 66, 1–16, doi:10.1016/S0034-4257(98)00031-5, 1998.
Jickells, T. D., An, Z. S., Andersen, K. K., Baker, A. R., Bergametti, G., Brooks, N., Cao, J. J., Boyd, P. W., Duce, R. A., Hunter, K. A., Kawahata, H., Kubilay, N., LaRoche, J., Liss, P. S., Mahowald, N., Prospero, J. M., Ridgwell, A. J., Tegen, I., and Torres, R.: Global iron connections between desert dust, ocean biogeochemistry, and climate, Science, 308, 67–71, doi:10.1126/science.1105959, 2005.
Kahn, R. A., Gaitley, B. J., Garay, M. J., Diner, D. J., Eck, T. F., Smirnov, A., and Holben, B. N.: Multiangle Imaging SpectroRadiometer global aerosol product assessment

ACPD
14, 31627–31674, 2014

by comparison with the Aerosol Robotic Network, J. Geophys. Res., 115, D23209, doi:10.1029/2010JD014601, 2010.
Kishcha, P., da Silva, A. M., Starobinets, B., and Pinhas, A.: Air pollution over the Ganges basin and northwest Bay of Bengal in the early postmonsoon season based on NASA MERRAero data, J. Geophys. Res.-Atmos., 19, 1555–1570, doi:10.1002/2013JD020328, 2014.
Koster, R. D., Suarez, M. J., Ducharne, A., Stieglitz, M., and Kumar, P.: A catchment-based approach to modeling land surface processes in a general circulation model: 1. Model structure, J. Geophys. Res.-Atmos., 105, 24809–24822, doi:10.1029/2000jd900327, 2000.
Lin, J.-T. and McElroy, M. B.: Impacts of boundary layer mixing on pollutant vertical profiles in the lower troposphere: Implications to satellite remote sensing, Atmos. Environ., 44, 1726–1739, doi:10.1016/j.atmosenv.2010.02.009, 2010.
Lin, S.-J.: A "Vertically Lagrangian" finite-volume dynamical core for global models, Mon. Weather Rev., 132, 2293–2307, doi:10.1175/1520-0493(2004)132<2293:avlfdc>2.0.CO;2, 2004.
Lock, A. P., Brown, A. R., Bush, M. R., Martin, G. M., and Smith, R. N. B.: A new boundary layer mixing scheme, Part I: Scheme description and single-column model tests, Mon. Weather Rev., 128, 3187–3199, doi:10.1175/1520-0493(2000)128<3187:anblms>2.0.CO;2, 2000.
Louis, J., Tiedtke, M., and Geleyn, J.: A short history of the PBL parameterization at ECMWF, workshop on planetary boundary layer parameterization, ECMWF, Reading, England, 5–27 November 1981, 59–79, 1982.
Mahowald, N: Aerosol indirect effect on biogeochemical cycles and climate, Science, 334, 6057, doi:10.1126/science.1207374, 2011.
Mahrt, L. and Vickers, D: Formulation of turbulent fluxes in the stable boundary layer, J. Atmos. Sci., 60, 2538–2548, doi:10.1175/1520-0469(2003)060<2538:FOTFIT>2.0.CO;2, 2003.
Marland, G. and Rotty, R. M.: Carbon dioxide emissions from fossil fuels: a procedure for estimation and results for 1950–1982, Tellus B, 36B, 232–261, doi:10.1111/j.1600-0889.1984.tb00245.x, 1984.
Marland, G., Boden, T. A., and Andres, R. J.: Global, regional, and national fossil fuel CO_2 emissions, in: Trends: A compendium of Data on Global Change, Carbon Dioxide Inf. Anal. Cent., Oak Ridge Natl. Lab., Oak Ridge, Tenn., available at: http://cdiac.ornl.gov/trends/emis/overview.html (last access: 11 April 2014), 2008.

ACPD
14, 31627–31674, 2014

McGrath-Spangler, E. L. and Denning, A. S.: Impact of entrainment from overshooting thermals on land–atmosphere interactions during summer 1999, Tellus B, 62, 441–454, doi:10.1111/j.1600-0889.2010.00482.x, 2010.

McGrath-Spangler, E. L. and Molod, A.: Comparison of GEOS-5 AGCM planetary boundary layer depths computed with various definitions, Atmos. Chem. Phys., 14, 6717–6727, doi:10.5194/acp-14-6717-2014, 2014.

McGrath-Spangler, E. L., Denning, A. S., Corbin, K. D., and Baker, I. T.: Sensitivity of land–atmosphere exchanges to overshooting PBL thermals in an idealized coupled model, J. Adv. Model. Earth Syst., 1, 14, doi:10.3894/JAMES.2009.1.14, 2009.

Molod, A., Takacs, L., Suarez, M. J., Bacmeister, J. T., Song, I.-S., and Eichmann, A.: The GEOS-5 atmospheric general circulation model: mean climate and development from MERRA to Fortuna, Technical Report Series on Global Modeling and Data Assimilation, 28, 115 pp., available at: http://gmao.gsfc.nasa.gov/pubs/docs/tm28.pdf (last access: 4 March 2014), 2012.

Moorthi, S. and Suarez, M. J.: Relaxed Arakawa–Schubert. A parameterization of moist convection for general circulation models, Mon. Weather Rev., 120, 978–1002, doi:10.1175/1520-0493(1992)120<0978:rasapo>2.0.CO;2, 1992.

O'Dell, C. W., Connor, B., Bösch, H., O'Brien, D., Frankenberg, C., Castano, R., Christi, M., Eldering, D., Fisher, B., Gunson, M., McDuffie, J., Miller, C. E., Natraj, V., Oyafuso, F., Polonsky, I., Smyth, M., Taylor, T., Toon, G. C., Wennberg, P. O., and Wunch, D.: The ACOS CO_2 retrieval algorithm – Part 1: Description and validation against synthetic observations, Atmos. Meas. Tech., 5, 99–121, doi:10.5194/amt-5-99-2012, 2012.

Ott, L. E., Pawson, S., Collatz, G. J., Gregg, W., Menemenlis, D., Brix, H., Rousseaux, C., Bowman, K., Liu, J., Eldering, A., Gunson, M., and Kawa, S. R.: Quantifying the observability of CO_2 flux uncertainty in atmospheric CO_2 records using products from NASA's Carbon Monitoring Flux Pilot Project, accepted for publication, J. Geophys. Res., 2014.

Parazoo, N. C., Denning, A. S., Kawa, S. R., Corbin, K. D., Lokupitiya, R. S., and Baker, I. T.: Mechanisms for synoptic variations of atmospheric CO_2 in North America, South America and Europe, Atmos. Chem. Phys., 8, 7239–7254, doi:10.5194/acp-8-7239-2008, 2008.

Parrish, D. D., Singh, H. B., Molina, L., and Madronich, S.: Air quality progress in North American megacities: a review, Atmos. Environ. 45, 7015–7025, doi:10.1016/j.atmosenv.2011.09.039, 2011.

ACPD
14, 31627–31674, 2014

Pérez, N., Pey, J., Cusack, M., Reche, C., Querol, X., Andrés, A., and Viana, M.: Variability of particle number, black carbon, and PM_{10}, $PM_{2.5}$, and PM_1 levels and speciation: influence of road traffic emissions on urban air quality, Aerosol Sci. Tech., 44, 487–499, doi:10.1080/02786821003758286, 2010.

Potter, C. S., Randerson, J. T., Field, C. B., Matson, P. A., Vitousek, P. M., Mooney, H. A., and Klooster, S. A.: Terrestrial ecosystem production: a process-oriented model based on global satellite and surface data, Global Biogeochem. Cy., 7, 811–842, doi:10.1029/93GB02725, 1993.

Putman, W. M. and Lin, S.-J.: Finite-volume transport on various cubed-sphere grids, J. Comput. Phys., 227, 55–78, doi:10.1016/j.jcp.2007.07.022, 2007.

Randerson, J. T., Thompson, M. V., Conway, T. J., Field, C. B., and Fung, I. Y.: Substrate limitations for heterotrophs: implications for models that estimate the seasonal cycle of atmospheric CO_2, Global Biogeochem. Cy., 10, 585–602, doi:10.1029/96GB01981, 1996.

Randles, C. A., Colarco, P. R., and da Silva, A.: Direct and semi-direct aerosol effects in the NASA GEOS-5 AGCM: aerosol–climate interactions due to prognostic vs. prescribed aerosols, J. Geophys Res.-Atmos., 118, 149–169, doi:10.1029/2012JD018388, 2013.

Remer, L. A., Kaufman, Y. J., Tanré, D., Mattoo, S., Chu, D. A., Martins, J. V., Li, R.-R., Ichoku, C., Levy, R. C., Kleidman, R. G., Eck, T. F., Vermote, E., and Holben, B. N.: The MODIS aerosol algorithm, products, and validation, J. Atmos. Sci., 62, 947–973, doi:10.1175/JAS3385.1, 2005.

Rienecker, M. M., Suarez, M. J., Todling, R., Bacmeister, J. T., Takacs, L., Liu, H.-C., Gu, W., Sienkiewicz, M., Koster, R., Gelaro, R., Stajner, I., and Nielsen, J. E.: The GEOS-5 data assimilation system – Documentation of versions 5.0.1, 5.1.0, and 5.2.0, Technical Report Series on Global Modeling and Data Assimilation, 101 pp., available at: http://gmao.gsfc.nasa.gov/pubs/docs/GEOS5_104606-Vol27.pdf (last access: 4 March 2014), 2008.

Rienecker, M. M., Suarez, M. J., Gelaro, R., Todling, R., Bacmeister, J., Liu, E., Bosilovich, M. G., Schubert, S. D., Takacs, L., Kim, G.-K., Bloom, S., Chen, J., Collins, D., Conaty, A., da Silva, A., Gu, W., Joiner, J., Koster, R. D., Lucchesi, R., Molod, A., Owens, T., Pawson, S., Pegion, P., Redder, C. R., Reichle, R., Robertson, F. R., Ruddick, A. G., Sienkiewicz, M., and Woollen, J.: MERRA: NASA's Modern-Era Retrospective Analysis for research and applications, J. Climate, 24, 3624–3648, doi:10.1175/jcli-d-11-00015.1, 2011.

ACPD
14, 31627–31674, 2014

Rosenfeld, D., Rudich, Y., Lahav, R.: Desert dust suppressing precipitation: a possible desertification feedback loop, Proc. Natl. Acad. Sci. USA, 98, 5975–5980, doi:10.1073/pnas.101122798, 2001.
Rossow, W. B. and Schiffer, R. A.: ISCCP cloud data products, B. Am. Meteorol. Soc., 72, 2–20, doi:10.1175/1520-0477(1991)072<0002:ICDP>2.0.CO;2, 1991.
Rossow, W. B. and Schiffer, R. A.: Advances in understanding clouds from ISCCP, B. Am. Meteorol. Soc., 80, 2261–2287, doi:10.1175/1520-0477(1999)080<2261:AIUCFI>2.0.CO;2, 1999.
Sandu, I., Beljaars, A., Bechtold, P., Mauritsen, T., and Balsamo, G.: Why is it so difficult to represent stably stratified conditions in numerical weather prediction (NWP) models?, J. Adv. Model Earth Syst., 5, 117–133, doi:10.1002/jame.20013, 2013.
Seidel, D. J., Ao, C. O., and Li, K.: Estimating climatological planetary boundary layer heights from radiosonde observations: comparison of methods and uncertainty analysis, J. Geophys. Res., 115, D16113, doi:10.1029/2009jd013680, 2010.
Seidel, D. J., Zhang, Y., Beljaars, A., Golaz, J.-C., Jacobson, A. R., and Medeiros, B.: Climatology of the planetary boundary layer over the continental United States and Europe, J. Geophys. Res.-Atmos., 117, D17106, doi:10.1029/2012jd018143, 2012.
Sinclair, V. A., Gray, S. L., and Belcher, S. E.: Boundary-layer ventilation by baroclinic life cycles, Q. J. Roy. Meteor. Soc., 134, 1409–1424, doi:10.1002/qj.293, 2008.
Sokolik, I. N. and Toon, O. B.: Direct radiative forcing by anthropogenic airborne mineral aerosols, Nature, 381, 681–683, doi:10.1038/381681a0 1996.
Troen, I. B. and Mahrt, L.: A simple model of the atmospheric boundary layer; Sensitivity to surface evaporation, Bound.-Lay. Meteorol., 37, 129–148, doi:10.1007/BF00122760, 1986.
van der Werf, G. R., Randerson, J. T., Giglio, L., Collatz, G. J., Mu, M., Kasibhatla, P. S., Morton, D. C., DeFries, R. S., Jin, Y., and van Leeuwen, T. T.: Global fire emissions and the contribution of deforestation, savanna, forest, agricultural, and peat fires (1997–2009), Atmos. Chem. Phys., 10, 11707–11735, doi:10.5194/acp-10-11707-2010, 2010.
Vogelezang, D. H. P. and Holtslag, A. A. M.: Evaluation and model impacts of alternative boundary-layer height formulations, Bound.-Lay. Meteorol., 81, 245–269, doi:10.1007/bf02430331, 1996.
Wunch, D., Wennberg, P. O., Toon, G. C., Connor, B. J., Fisher, B., Osterman, G. B., Frankenberg, C., Mandrake, L., O'Dell, C., Ahonen, P., Biraud, S. C., Castano, R., Cressie, N., Crisp, D., Deutscher, N. M., Eldering, A., Fisher, M. L., Griffith, D. W. T., Gunson, M.,

ACPD
14, 31627–31674, 2014

Heikkinen, P., Keppel-Aleks, G., Kyrö, E., Lindenmaier, R., Macatangany, R., Mendonca, J., Messerschmidt, J., Miller, C. E., Morino, I., Notholt, J., Oyafuso, F. A., Rettinger, M., Robinson, J., Roehl, C. M., Salawitch, R. J., Sherlock, V., Strong, K., Sussmann, R., Tanaka, T., Thompson, D. R., Uchino, O., Warneke, T., and Wofsy, S. C.: A method for evaluating bias in global measurements of CO_2 total columns from space, Atmos. Chem. Phys., 11, 20899–20946, doi:10.5194/acpd-11-20899-2011, 2011.

Yevich, R. and Logan, J. A.: An assessment of biofuel use and burning of agricultural waste in the developing world, Global Biogeochem. Cy., 17, 1095, doi:10.1029/2002GB001952, 2003.

Yokota, T., Oguma, H., Morino, I., and Inoue, G.: A nadir looking SWIR FTS to monitor CO_2 column density for Japanese GOSAT project, Proc. Twenty-Fourth Int. Sympo. on Space Technol. Sci. (Selected Papers), Miyazaki, Japan, 30 May–6 June 2004, 887–889, 2004.

ACPD
14, 31627–31674, 2014

Table 1. Summary of PBL depth methods.

Method/ Experiment	Abbreviation	Description
1	K_h: 2	Uses K_h and a threshold of 2 $m^2 s^{-1}$
2	K_h: 10 %	Uses K_h and a threshold equal to 10 % of the column maximum
3	Bulk *Ri*	Uses the bulk Richardson number described by Seidel et al. (2012) and a critical value of 0.25

ACPD
14, 31627–31674, 2014

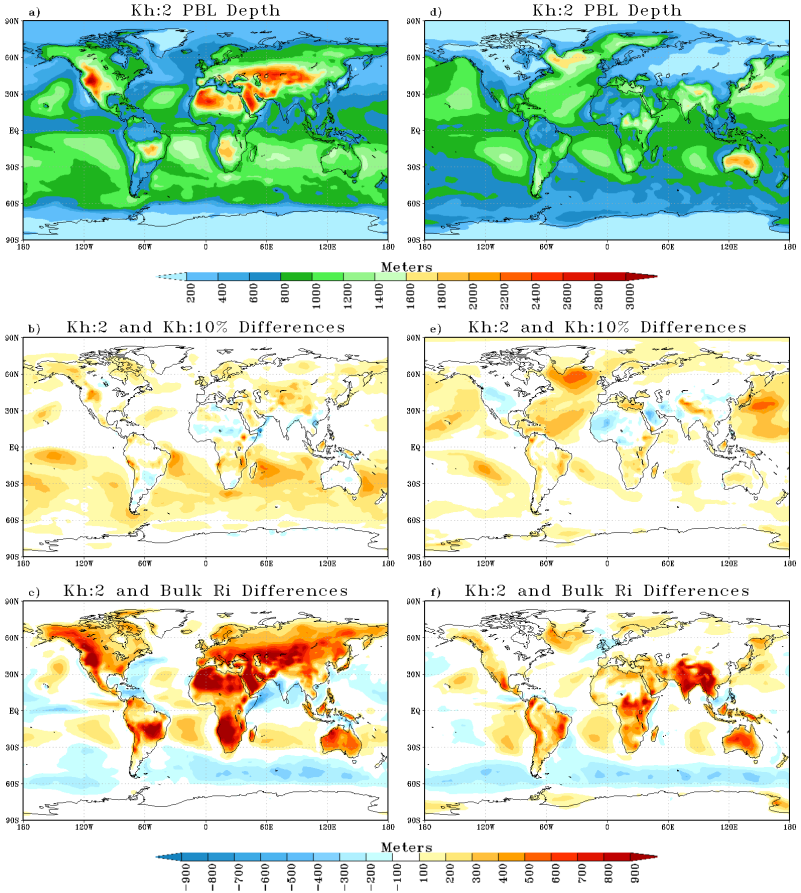

Figure 1. Seasonal mean PBL depth estimated by the K_h: 2 PBL depth estimation method for JJA **(a)** and DJF **(d)**, the differences between the K_h: 2 and K_h: 10 % methods during JJA **(b)** and DJF **(e)**, and the differences between the K_h: 2 and Bulk *Ri* methods during JJA **(c)** and DJF **(f)**.

ACPD
14, 31627–31674, 2014

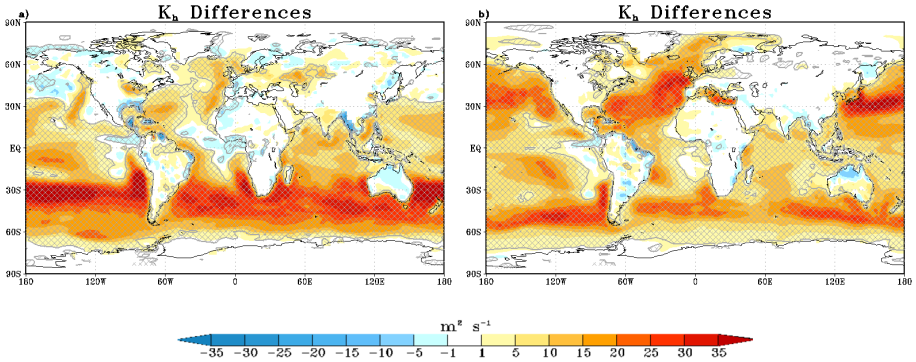

Figure 2. Seasonal mean turbulent eddy diffusion coefficient at 925 hPa differences (Method 3 minus Method 2) for JJA **(a)** and DJF **(b)**. Hatch marks represent significance at the 90 % level using the student's *t* test. Crosshatch marks represent significance at the 95 % level.

ACPD
14, 31627–31674, 2014

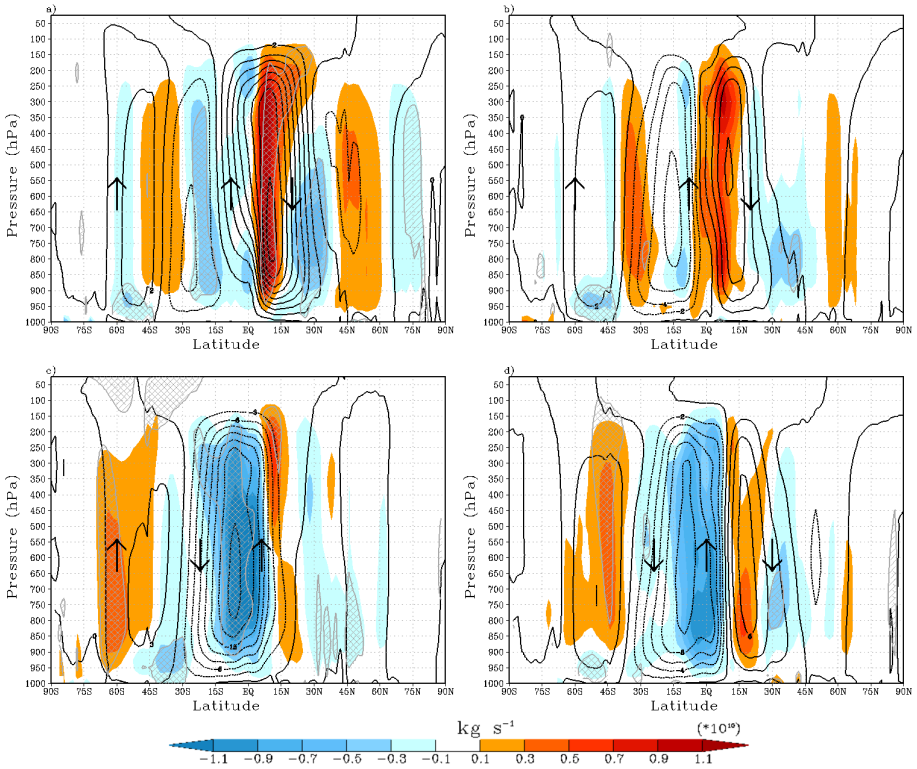

Figure 3. Seasonal mean difference (Method 3 minus Method 2; shaded) and average (contours) mean meridional circulation for **(a)** DJF, **(b)** MAM, **(c)** JJA, and **(d)** SON. Positive (negative) values are represented by solid (dashed) lines. Arrows indicate the sense of the circulation. Hatch marks represent significance at the 90 % level using the student's *t* test. Crosshatch marks represent significance at the 95 % level.

ACPD
14, 31627–31674, 2014

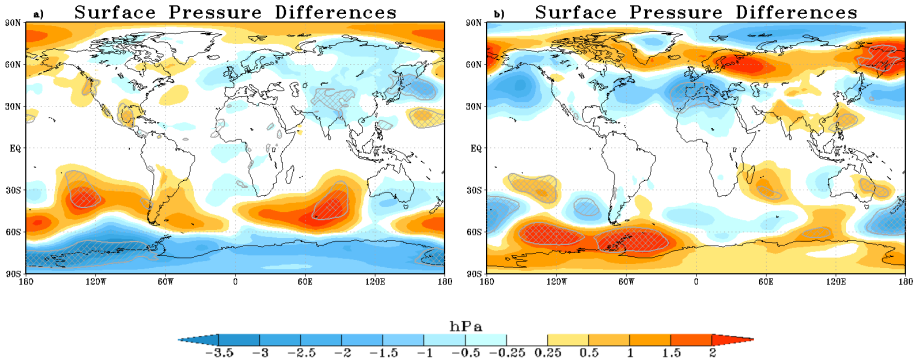

Figure 4. Seasonal mean surface pressure differences (Method 3 minus Method 2) for JJA **(a)** and DJF **(b)**. Hatch marks represent significance at the 90 % level using the student's *t* test. Crosshatch marks represent significance at the 95 % level.

ACPD
14, 31627–31674, 2014

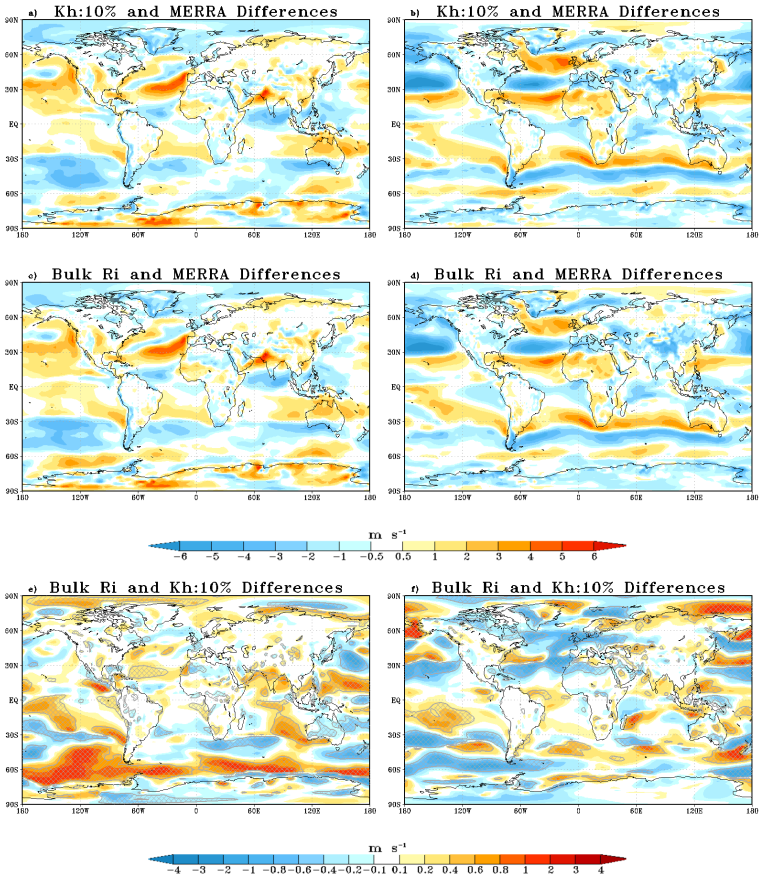

Figure 5. Seasonal mean 10 m wind speed differences. Method 2 minus MERRA for JJA **(a)** and DJF **(b)**, Method 3 minus MERRA for JJA **(c)** and DJF **(d)**, and Method 3 minus Method 2 for JJA **(e)** and DJF **(f)**. Hatch marks on the bottom plots represent significance at the 90 % level using the student's *t* test. Crosshatch marks represent significance at the 95 % level.

ACPD
14, 31627–31674, 2014

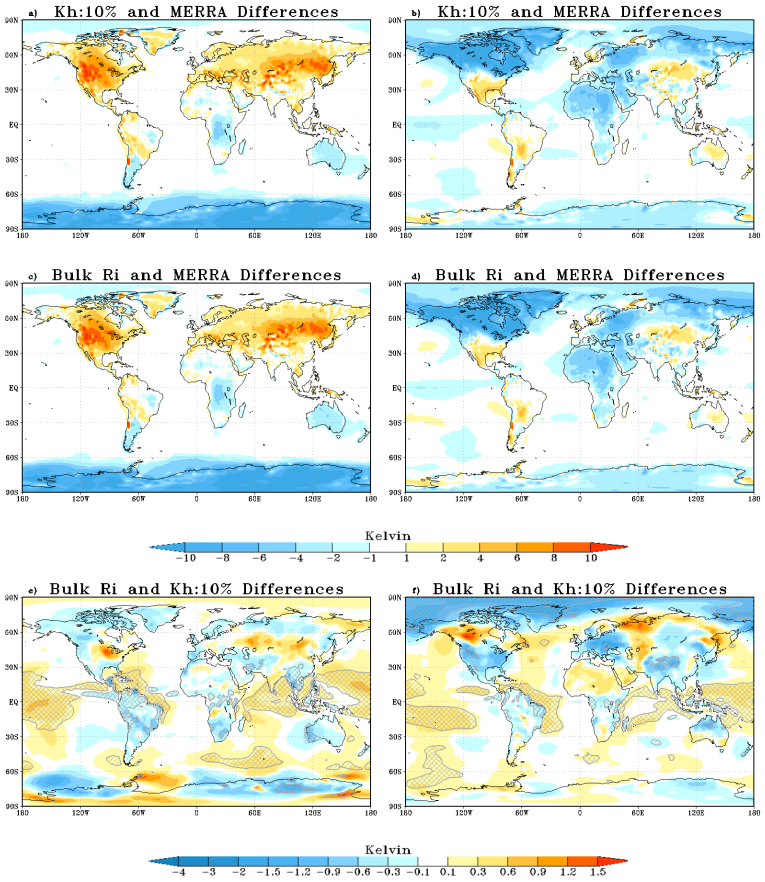

Figure 6. Seasonal mean 2 m temperature differences. Method 2 minus MERRA for JJA **(a)** and DJF **(b)**, Method 3 minus MERRA for JJA **(c)** and DJF **(d)**, and Method 3 minus Method 2 for JJA **(e)** and DJF **(f)**. Hatch marks on the bottom plots represent significance at the 90 % level using the student's *t* test. Crosshatch marks represent significance at the 95 % level.

ACPD
14, 31627–31674, 2014

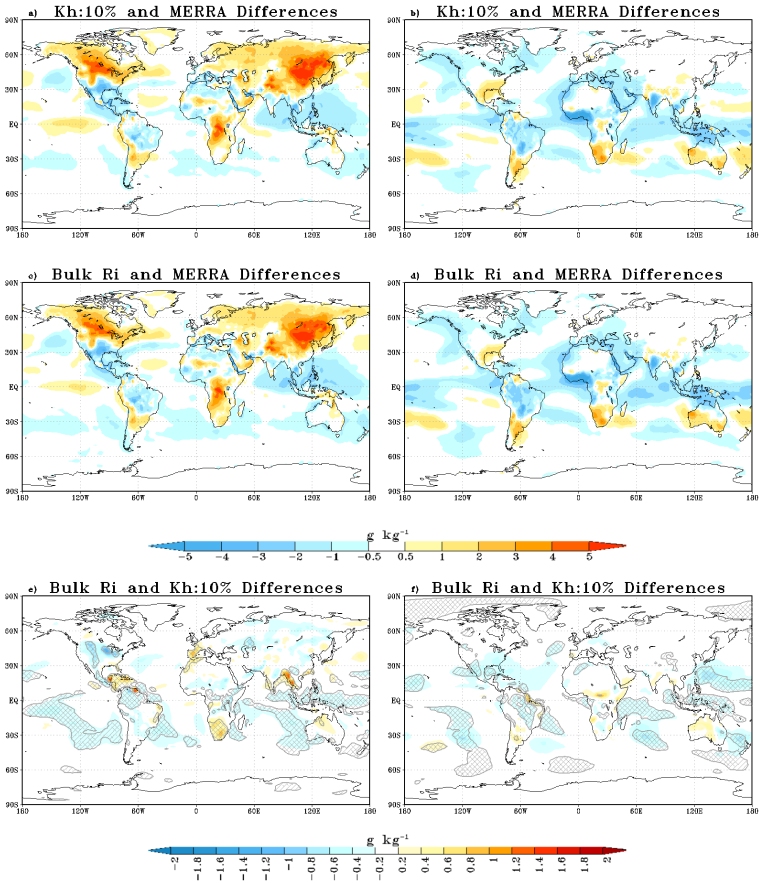

Figure 7. Seasonal mean 2 m specific humidity differences. Method 2 minus MERRA for JJA **(a)** and DJF **(b)**, Method 3 minus MERRA for JJA **(c)** and DJF **(d)**, and Method 3 minus Method 2 for JJA **(e)** and DJF **(f)**. Hatch marks on the bottom plots represent significance at the 90 % level using the student's *t* test. Crosshatch marks represent significance at the 95 % level.

ACPD
14, 31627–31674, 2014

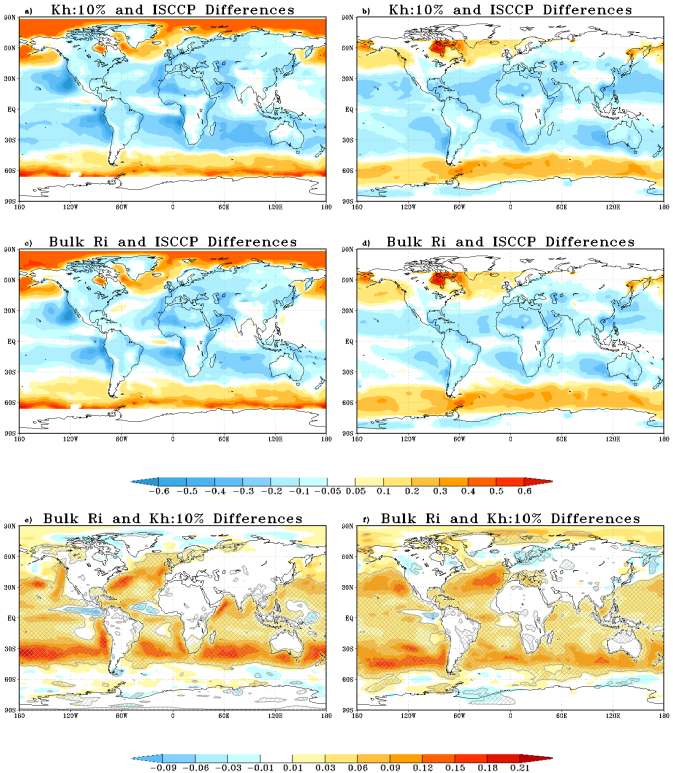

Figure 8. Seasonal mean low level cloud fraction differences. Method 2 minus ISCCP for JJA **(a)** and DJF **(b)**, Method 3 minus ISCCP for JJA **(c)** and DJF **(d)**, and Method 3 minus Method 2 for JJA **(e)** and DJF **(f)**. Hatch marks on the bottom plots represent significance at the 90 % level using the student's *t* test. Crosshatch marks represent significance at the 95 % level.

ACPD
14, 31627–31674, 2014

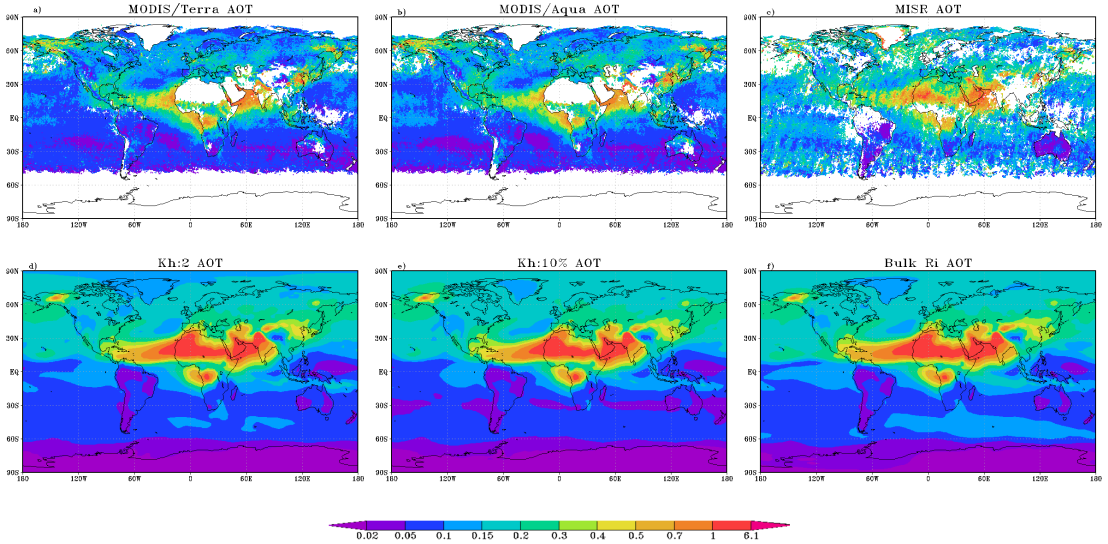

Figure 9. Jul 2009 monthly mean aerosol optical thickness observations from the MODIS instruments on the Terra (global mean = 0.1277, SD = 0.0645; **(a)** and Aqua (global mean = 0.1339, SD = 0.0750; **(b)** satellites and from the MISR (global mean = 0.1808, SD = 0.0617; **(c)** instrument on Terra. Monthly average aerosol optical thickness simulated by the GEOS-5 model using the turbulent eddy diffusion coefficient method and a threshold of $2\,m^2\,s^{-1}$ (Method 1, global mean = 0.1985, SD = 0.0796; **(d)**, a threshold of 10 % of the column maximum (Method 2, global mean = 0.1943, standard deviation = 0.0774; **(e)**, and the bulk Richardson number method (Method 3, global mean = 0.2153, SD = 0.0880; **(f)**.

ACPD
14, 31627–31674, 2014

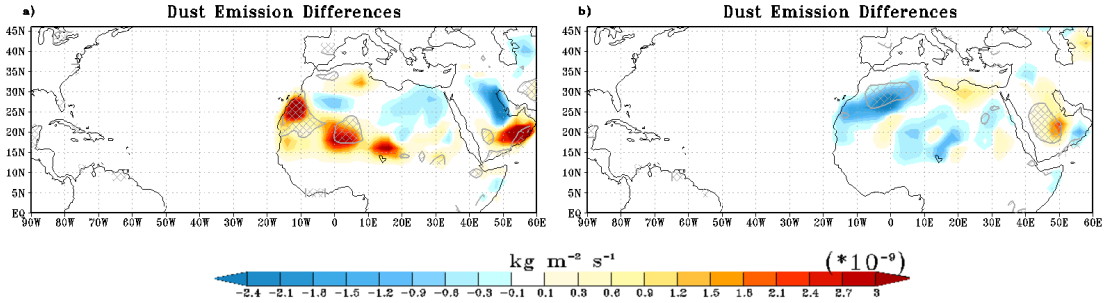

Figure 10. Seasonal mean dust emission differences (Method 3 minus Method 2) for JJA **(a)** and DJF **(b)**. Average dust emission in the emitting region is about 1×10^{-8} kg m^{-2} s^{-1}. Hatch marks represent significance at the 90 % level using the student's t test. Crosshatch marks represent significance at the 95 % level.

ACPD
14, 31627–31674, 2014

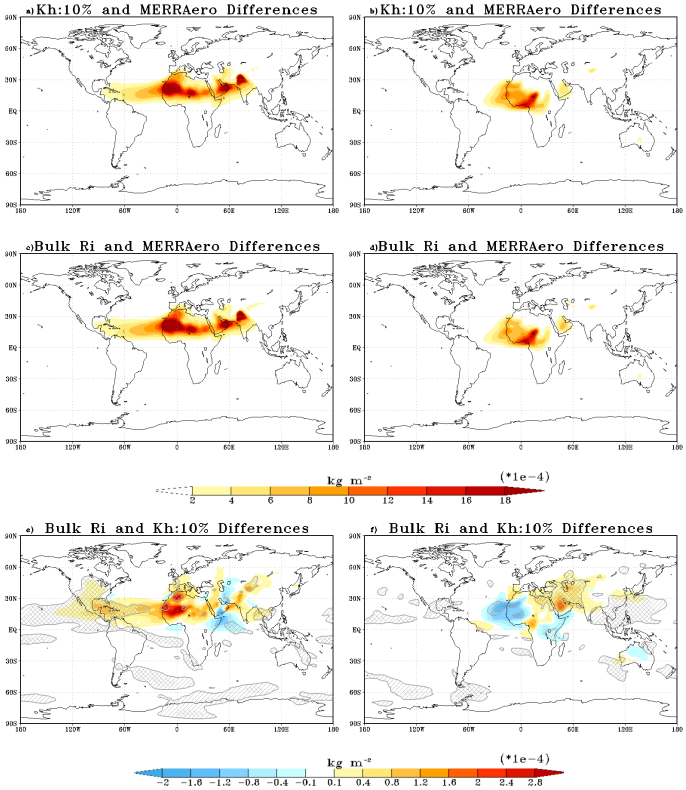

Figure 11. Seasonal mean column dust differences. Method 2 minus MERRAero for JJA **(a)** and DJF **(b)**, Method 3 minus MERRAero for JJA **(c)** and DJF **(d)**, and Method 3 minus Method 2 for JJA **(e)** and DJF **(f)**. Global mean column dust concentrations in the free-running models is about 1.2×10^{-4} kg m^{-2} during JJA and about 5.7×10^{-5} kg m^{2} during DJF. Hatch marks on the bottom plots represent significance at the 90 % level using the student's t test. Crosshatch marks represent significance at the 95 % level.

ACPD
14, 31627–31674, 2014

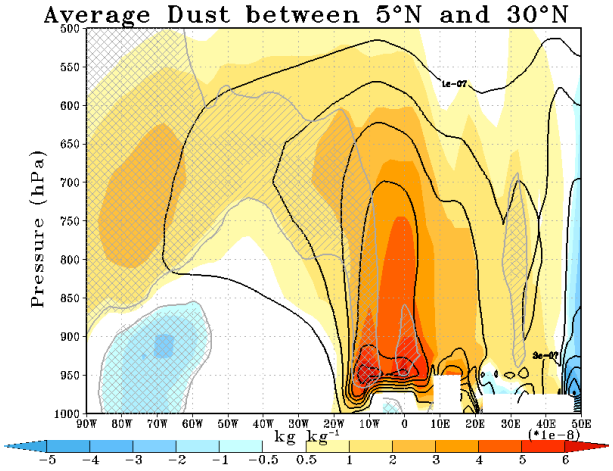

Figure 12. Seasonal mean dust differences (shaded, Method 3 minus Method 2) and mean dust concentration (black contours) for JJA averaged from 5° N to 30° N. Average concentration is about 1.6×10^{-7} kg kg^{-1}. Hatch marks represent significance at the 90 % level using the student's t test. Crosshatch marks represent significance at the 95 % level.

ACPD
14, 31627–31674, 2014

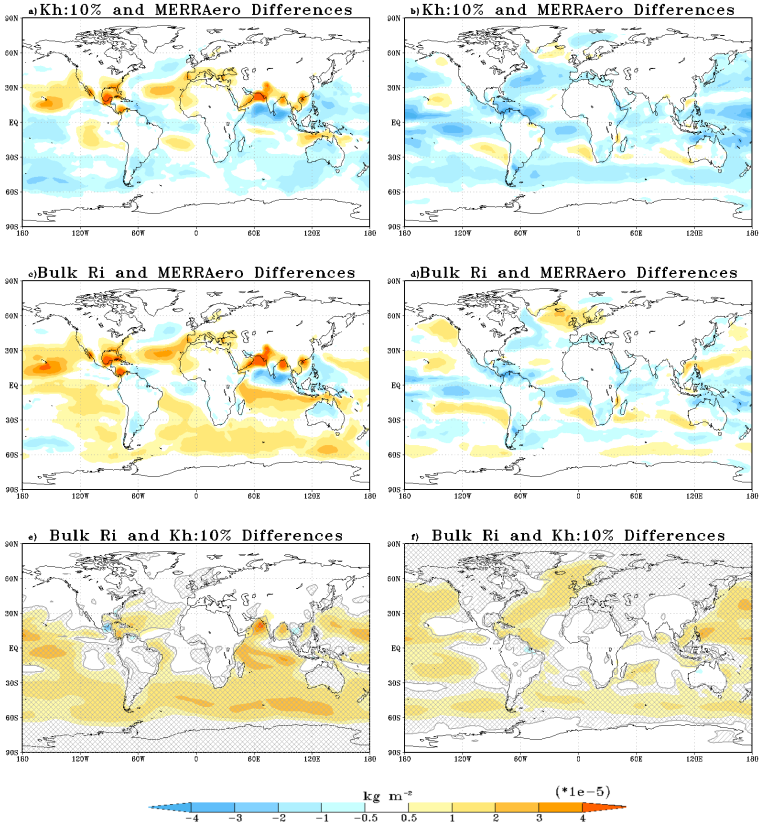

Figure 13. Seasonal mean column sea salt differences. Method 2 minus MERRAero for JJA **(a)** and DJF **(b)**, Method 3 minus MERRAero for JJA **(c)** and DJF **(d)**, and Method 3 minus Method 2 for JJA **(e)** and DJF **(f)**. Hatch marks on the bottom plots represent significance at the 90 % level using the student's *t* test. Crosshatch marks represent significance at the 95 % level.

ACPD
14, 31627–31674, 2014

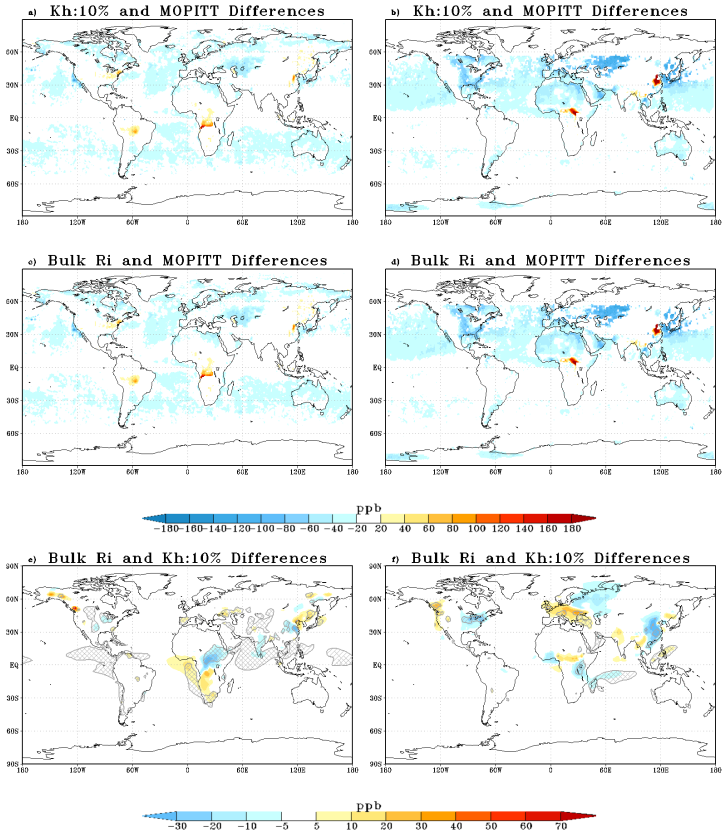

Figure 14. Seasonal mean surface CO differences. Method 2 minus MOPITT for JJA **(a)** and DJF **(b)**, Method 3 minus MOPITT for JJA **(c)** and DJF **(d)**, and Method 3 minus Method 2 for JJA **(e)** and DJF **(f)**. Model comparisons to MOPITT have been sampled using the MOPITT averaging kernel. Hatch marks on the bottom plots represent significance at the 90 % level using the student's *t* test. Crosshatch marks represent significance at the 95 % level.

ACPD
14, 31627–31674, 2014

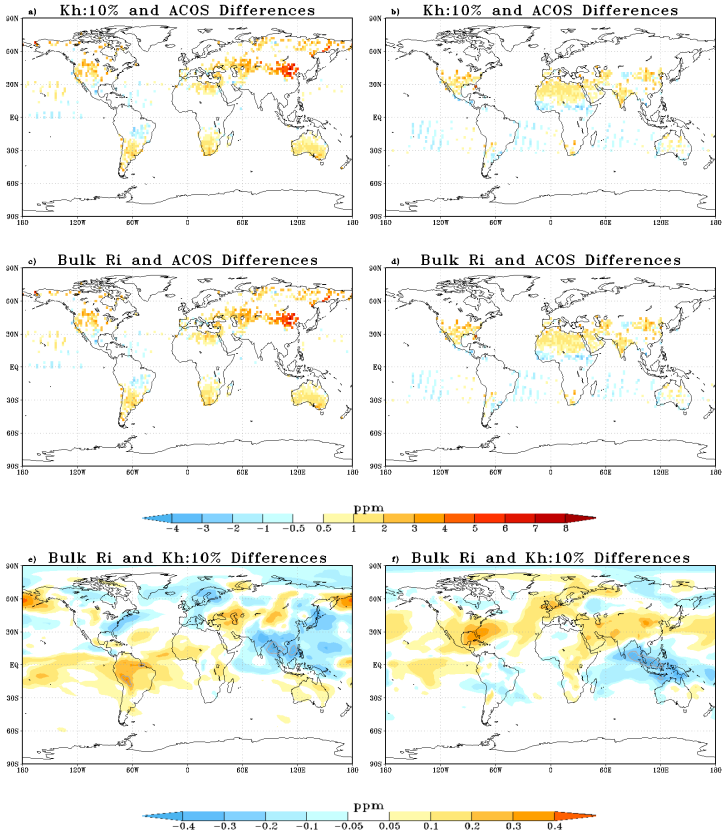

Figure 15. Seasonal mean column CO_2 differences. Method 2 minus ACOS for JJA **(a)** and DJF **(b)**, Method 3 minus ACOS for JJA **(c)** and DJF **(d)**, and Method 3 minus Method 2 for JJA **(e)** and DJF **(f)**. Model comparisons to ACOS have been sampled using the ACOS averaging kernel. Hatch marks on the bottom plots represent significance at the 90 % level using the student's *t* test. Crosshatch marks represent significance at the 95 % level.

ACPD
14, 31627–31674, 2014

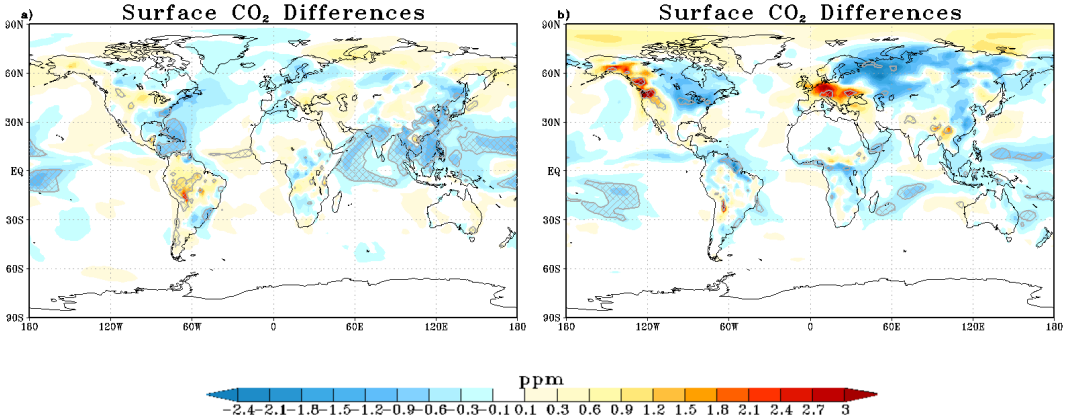

Figure 16. Seasonal mean surface CO_2 differences (Method 3 minus Method 2) for JJA **(a)** and DJF **(b)**. Hatch marks represent significance at the 90 % level using the student's *t* test. Crosshatch marks represent significance at the 95 % level.

ACPD
14, 31627–31674, 2014

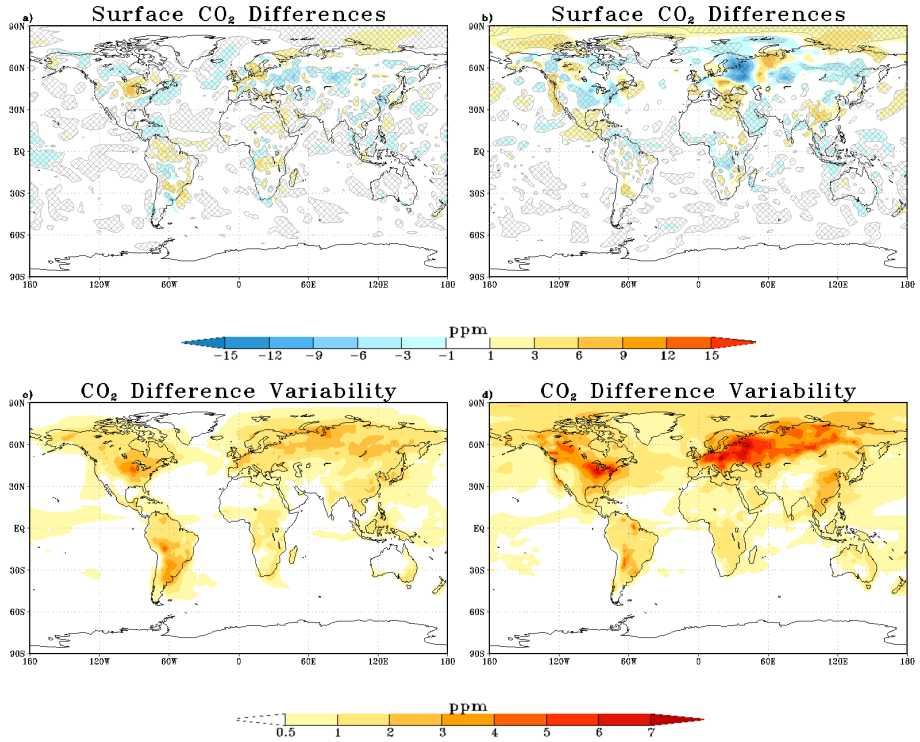

Figure 17. Surface CO_2 differences (Method 3 minus Method 2) for **(a)** 1 : 30Z 1 Jul 2009 and **(b)** 1 : 30Z 1 Jan 2010. Hatch marks represent significance at the 90 % level using the student's *t* test. Crosshatch marks represent significance at the 95 % level. SD of surface CO_2 differences (Method 3 minus Method 2) for **(c)** Jul 2009 and **(d)** Jan 2010.

ACPD
14, 31627–31674, 2014